PCCP
Physical Chemistry Chemical Physics

Accepted Manuscript

This article can be cited before page numbers have been issued, to do this please use: C. J. Pereyra, Y. Di iorio, M. Berruet, M. Vazquez and R. Marotti, *Phys. Chem. Chem. Phys.*, 2019, DOI: 10.1039/C9CP04256C.

View Article Online
DOI: 10.1039/C9CP04256C

Journal Name

ARTICLE TYPE

Cite this: DOI: 00.0000/xxxxxxxxxx

Carrier Recombination and Transport Dynamics in Superstrate Solar Cells analyzed by modeling the Intensity Modulated Photoresponses.

Carlos J. Pereyra,*[a,b] Yesica Di Iorio,[b] Mariana Berruet,[b] Marcela Vazquez,[b] and Ricardo E. Marotti [a]

Received Date
Accepted Date

DOI: 00.0000/xxxxxxxxxx

The dynamics of carrier recombination and transport of two $CuInS_2$ superstrate solar cells was studied by intensity modulated photovoltage and photocurrent spectroscopy (IMVS and IMPS respectively). For the analysis of the resulting data two different approaches were implemented. In the first approach, the typically used analysis in Dye Sensitized Solar Cells (DSSC) was adapted to obtain the characteristics times of the processes involved. The second approach was based on the fittings of both the IMVS and IMPS data to the solution of the continuity equation. These fittings allow the calculation of different dynamic parameters of the cells. Moreover, consistency between the obtained parameters was observed, in good agreement with the typical analysis for DSSC. The resulting dynamics was associated with the presence and distribution of defect states among the samples. Moreover, from the performed analysis, a relation between the results and the post treatment applied to the solar cells could be established. The difference in the dynamics of the cells is mainly observed in the difference between the electron lifetimes of both solar cells.

1 Introduction

Chalcopyrite based semiconductors are extensively studied materials for thin films solar cells due to their interesting optical properties. Particularly, in the system $CuInSe_{2-2y}S_{2y}$ the direct bandgap can be tuned from 1.02 to 1.52 eV as **y** increases.[1] This is because sulfur addition to $CuInSe_2$ leads to an energetic reduction of the valence band maximum and to an enhancement of the conduction band minimum.[2,3] Thus, sulfur extends the interface bandgap and thereby depresses interface recombination. In addition, it has been shown that sulfur leads to an increased carrier lifetime in the absorber.[4] A full replacement of Se by S leads the ternary $CuInS_2$ (CIS). This compound is particularly interesting because it typically exhibits bandgap energies between 1.47 and 1.57 eV,[5–7] which are close to the optimal bandgap in the Shockley-Queisser limit.[8] The performance of solar cells combining In_2S_3 and $CuInS_2$ as buffer and absorbing layers respectively, have been studied In previous publications.[4,9] The indirect bandgap of In_2S_3 is beneficial in terms of current collection but appears problematic in terms of interface recombination.[4,9] Superstrate configuration is chosen so that all the materials could be prepared using inexpensive and eco-friendly techniques, based on solution processed deposition methods and non-toxic materials, avoiding vacuum high temperature Cd-containing layers.[10–13]

The goal of this work is to use Intensity Modulated Photovoltage Spectroscopy (IMVS) and Intensity Modulated Photocurrent Spectroscopy (IMPS) to study the inner dynamics of two types of superstrate solar cells based on $FTO/TiO_2/In_2S_3/CuInS_2$/graphite. The single difference between them is the $CuInS_2$ nature, i.e, the defect state density as a consequence of chosen deposition method and subsequent treatments. The IMVS and IMPS techniques are very useful to elucidate the behavior of the recombination, transport and extraction of the photogenerated charge carriers within the solar cell.[14–20] IMVS and IMPS can be used to measure the real and imaginary components of the photovoltage and photocurrent generated by a modulation in the optical excitation of the solar cell.[14–20] The working principle of these techniques is similar and complementary to that of impedance spectroscopy where the excitation is originated in a modulation of the applied voltage on the device instead of light modulation.[21–23] IMVS and IMPS are commonly used in semiconductor/electrolyte interfaces,[24,25] water splitting systems,[22] DSSC or solid states solar cells to elucidate the transport and recombination characteristic times of the cells.[15,17,26–28] However, the analyses are restricted to the solely determination of the characteristics times, or to the fitting of only the IMVS or IMPS data with the solution of the continuity equation.[15,17,21,26–28] A complementary analysis of the resulting spectra was implemented

[a] Instituto de Física, Facultad de Ingeniería, Universidad de la República, Julio Herrera y Reissig 565, C.C. 30, 11000 Montevideo, Uruguay. E-mail: jpereyra@fing.edu.uy
[b] División Electroquímica Aplicada, INTEMA, Facultad de Ingeniería, CONICET-Universidad Nacional de Mar del Plata, Colon 10850, 7600, Mar del Plata, Argentina.

View Article Online
DOI: 10.1039/C9CP04256C

and both the IMVS and IMPS signals were explicitly considered. The first approach was based on the shape of the spectra in the Nyquist representation and therefore analyzed assuming a relaxation time process in the solar cell for both IMVS and IMPS. The second approach was based on the fitting of the spectra with the solution of the continuity equation in correspondence with the experimental conditions set in the solar cells at the time of the measurements. By properly choosing the boundary conditions in the continuity equation, both the IMVS and IMPS spectra could be fitted for the same set of parameters of the solar cell (diffusion and lifetime constants, absorption coefficient and thickness among others).[26] The results of these different fitting strategies were also compared for consistency purposes and a good agreement was obtained.

2 Theory

In order to model the IMVS and IMPS responses of the different solar cells the continuity equation for the electron density (δn(x,t)) within the solar cells is solved. The cell should be optically excited with a sinusoidal light signal of angular frequency ω and intensity $I(\omega,t)$

$$I(\omega,t) = I_0 + I_A cos(\omega t) \tag{1}$$

where I_0 is the mean value and I_A the modulation component. Moreover, for simplicity, the solar cell will be modeled as a one layer cell of thickness **d** and absorption coefficient α (see Fig.1). Under these conditions the continuity equation can be written as

$$\frac{\partial(\delta n(x,t))}{\partial t} = \alpha I_A exp(-\alpha x) exp(j\omega t) + D_e \frac{\partial^2(\delta n(x,t))}{\partial x^2} - \frac{\delta n(x,t)}{\tau_e} - k_{trap}\delta n(x,t) + k_{detrap} N_r(x,t)\ 0 < x < d \tag{2}$$

where x is the depth coordinate in the cell, D_e and τ_e are the diffusion and lifetime constant respectively. Also, k_{trap} and k_{detrap} are the electron trapping and detrapping rates by defect states within the solar cell. As these two last processes involve the participation of defect states, the density of occupied defect states (N_r) should be added and the equation for occupancy of the defect states dynamic should also be solved.

$$\frac{\partial N_r(x,t)}{\partial t} = k_{trap}\delta n(x,t) - k_{detrap} N_r(x,t)\ 0 < x < d \tag{3}$$

If a recombination process for electrons in trap states is included, an extra term should be added involving a new parameter associated with the characteristic time of the recombination process.[19] For simplicity, no recombination processes of electrons from the trap state to the valence band are considered in Equation 3. Finally, for the complete solution of the previous equations the boundary conditions for δn(x,t) are needed

$$D_e \frac{\partial(\delta n(x,t))}{\partial x}|_{x=0} = k_{sep}\delta n(x,t)|_{x=0} \tag{4}$$

$$D_e \frac{\partial(\delta n(x,t))}{\partial x}|_{x=d} = 0 \tag{5}$$

where k_{sep} represents the electron extraction constant at the interface between the cell and the electron-selective contact at $x = 0$. By appropriately choosing the value of k_{sep}, the cell working condition could be defined: open circuit conditions can be obtained when $k_{sep} = 0$ and short circuit conditions when $k_{sep} \neq 0$. Moreover, in short circuit conditions, low values of k_{sep} correspond to kinetic limited process while high k_{sep} values lead to diffusion limited process at the interface[19]. As the optical excitation is modulated, all the photogenerated quantities involved are expected to be modulated. Therefore, by fixing the values of k_{sep} in Equation 4 the solution for IMVS and IMPS for the same cell can be obtained. By solving Equation 2 and Equation 3 for these components, the modulated short circuit current ($J_{SC}(\omega)$) and open circuit potential ($V_{OC}(\omega)$) components can be calculated. Details of the calculation showing the solution of Equation 2 and Equation 3 are already available in the literature.[18,19,25,27,29] The results for $J_{SC}(\omega)$ and $V_{OC}(\omega)$ are

$$J_{SC}(\omega) = k_{sep}\frac{\alpha I_A}{(\beta^2-\alpha^2)} \frac{2\alpha exp(-\alpha d) + \beta(exp(\beta d) - exp(-\beta d)) - \alpha(exp(\beta d) + exp(-\beta d))}{\beta D_e(exp(\beta d) - exp(-\beta d)) + k_{sep}(exp(\beta d) + exp(-\beta d))} \tag{6}$$

$$V_{OC}(\omega) \propto \frac{\alpha I_A}{D_e(\beta^2-\alpha^2)} \left[1 + \frac{\alpha(2exp(-\alpha d) - exp(\beta d) - exp(-\beta d))}{\beta(exp(\beta d) - exp(-\beta d))}\right] \tag{7}$$

Where γ is frequency dependent factor

$$\gamma^2 = \left(\frac{1}{\tau_e} - \frac{k_{detrap}k_{trap}}{k_{detrap} + j\omega} + k_{trap} + j\omega\right) \tag{8}$$

and β is defined as $\beta^2 = \frac{\gamma^2}{D_e}$

If no defect states are considered, a simple version of Equation 2 can be used, since no equation for the occupancy of defect states is needed.

$$\frac{\partial(\delta n(x,t))}{\partial t} = \alpha I_A exp(-\alpha x) exp(j\omega t) + D_e \frac{\partial^2(\delta n(x,t))}{\partial^2 x} - \frac{\delta n(x,t)}{\tau_e} \tag{9}$$

Also, for the defect-free cell, a similar and simpler solution can be obtained by replacing γ by

$$\gamma^2 = \left(\frac{1}{\tau_e} + j\omega\right) \tag{10}$$

The net effect of the trap states could be interpreted by defining two new effective parameters as substitutes of the diffusion and lifetime constants (D_{ef} and τ_{ef} respectively). Therefore, the dynamics of a cell with trap states can be understood as the dynamics of a trap-free cell with effective diffusion and lifetime constants. By comparing Equation 8 and Equation 10 these two new parameters can be defined as[19]:

View Article Online
DOI: 10.1039/C9CP04256C

$$D_{ef} = \frac{D_e}{1 + \frac{k_{detrap} k_{trap}}{k_{detrap}^2 + \omega^2}} \tag{11}$$

$$\frac{1}{\tau_{ef}} = \frac{1}{\tau_e} + k_{trap}\left(1 - \frac{k_{detrap}^2}{k_{detrap}^2 + \omega^2}\right) \tag{12}$$

From the two previous expressions it is possible to observe that the main consequences of the trap states are the decrease of the diffusion constant and the increase of the recombination rate of electrons in the cell (τ_{ef}^{-1} increases). These factors contribute to an overall degradation of the inner dynamics within the cell, which has already been pointed out in the literature.[19] It is important to notice that, in the trap-free scenario, Equation 9 is responsible for the dynamics of this solar cells. Therefore, both the IMVS and IMPS responses could be obtained as a function of the same parameters D_{ef}, τ_{ef}, α, $\mathbf{d}$ and k_{sep} by the careful selection of k_{sep} in the boundary conditions (Equation 4). Within this approach, the same equation can be used for the analysis of both the IMVS and IMPS responses of the cell, providing further certainty in the parameter determination.

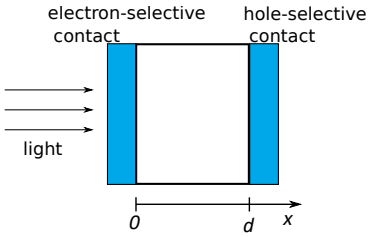

Fig. 1 Scheme of the solar cells considered in the present calculation.

3 Results

Figure 2a shows the GXRD of cells SCa and SCb. In both diffractograms the peaks are sharp and in good agreement with those in the diffraction cards of their components (TiO_2, PDF 21-1272 and $CuInS_2$, PDF 27-0159). The unmarked peak at 30.40 ° 2θ corresponds to reflections of K_β radiation with (101) plane FTO substrate. The peaks of the chalcopyrite structure in the two cells can be compared and reveal a pronounced broadening of the peak at 27.81 ° 2θ corresponding to the (112) plane CIS in the SCb sample. This can be attributed to the different route synthesis of the CIS films but mainly to the different annealing treatments. From the full line broadening at half the maximum intensity (FWHM) of the (112) plane signal the crystallite sizes can be estimated applying the Scherrer's equation. These are 20 and 12 nm for SCa and SCb respectively. As expected the increase of the crystallite size was accomplished with the increase of the crystalline degree associated basically to the higher temperature of the annealing treatment.

Raman spectroscopy can be used as a complementary technique to GXRD to confirm the composition and quality of the CIS films. The spectra measured with 785 nm excitation wavelength can be observed in Figure 2b, and shows a strong increment in the width of the CIS peaks in cell SCb expected due to the higher crystallinity of cell SCa. Therefore, both the high temperature of the thermal treatment and the incorporation of an etching stage can be responsible for the higher crystal quality and the lower proportion of undesired binary phases in the CIS layer of cell SCa compared with the CIS layer in cell SCb.

In Figure 3 the IMVS and IMPS responses ($H_{IMVS,IMPS}(\omega)$) for solar cells SCa and SCb in the Nyquist representation (imaginary vs. real parts of the $H_{IMVS,IMPS}(\omega)$ response) are presented, each curve corresponds with different values of I_0. Figure 3a and Figure 3b present the IMVS responses while Figure 3c and Figure 3d show the IMPS responses of cells SCa and SCb respectively. Every spectrum exhibits only one cycle in the complex plane. Also the cycles evolve from high to small values of the real part of the H_{IMVS} response as the frequency increases. In Figure 3c and Figure 3d a unique cycle is also observed and the size of the cycle decreases as I_0 increases. Moreover, as in the H_{IMVS} signal, the same evolution of the cycle with the frequency is observed. However, for high frequency values an important distortion from the semicircular shape of the spectra is observed. This distortion is usually observed in dye sensitized solar cells (DSSC) when the charge extraction process is dominated or limited by the diffusion process of charge carriers to the cell interface.[19,29,30] For the diffusion limited cases the Nyquist plots of H_{IMPS} usually present a high frequency tendency to the origin along a straight line with a 45° slope (the dashed magenta line in Figure 3c).[19,29,30] In this case, SCa presents the typical diffusion limited dynamics while SCb presents a kinetically limited dynamic evidenced by the semicircular shape of the IMPS Nyquist plot.[19,29,30]

As the Nyquist plots of the solar cells in the complex plane show one cycle, only one characteristic time constant is expected in $H_{IMVS,IMPS}(\omega)$. Typically, one cycle in the Nyquist plots is analyzed by a relaxation time $\tau_{IMVS,IMPS}$ function[15,17–19,29–31]

$$H_{IMVS,IMPS}(\omega) = \frac{A}{1 + j\omega\tau_{IMVS,IMPS}} \tag{13}$$

where A is an amplitude constant, τ_{IMVS} is typically associated with the characteristic recombination or lifetime time. On the other hand, τ_{IMPS} is commonly associated with the characteristic transport or transit time for the carriers in the cell ($\tau_{transit}$)[18,31] due to the following relation

$$\frac{1}{\tau_{IMPS}} = \frac{1}{\tau_{IMVS}} + \frac{1}{\tau_{transit}} \tag{14}$$

As generally $\tau_{IMVS} \gg \tau_{transit}$[31], therefore τ_{IMPS} could be associated with the characteristic transport or transit time in the cell. Finally, another parameter of interest in the dynamics of the solar cell that can be obtained from the $H_{IMVS,IMPS}(\omega)$ spectra is the charge collection efficiency (η_{CC}), which is the efficiency of the recollection of photogenerated charge carriers within the solar cell.[18,32] If independence between the different recombination processes and linearity on the recombination and extraction rates with the density of carriers are assumed, then η_{CC} can be calculated as

$$\eta_{CC} = 1 - \frac{\tau_{IMPS}}{\tau_{IMVS}} \tag{15}$$

For the analysis of the different $H_{IMVS,IMPS}(\omega)$ responses,

View Article Online
DOI: 10.1039/C9CP04256C

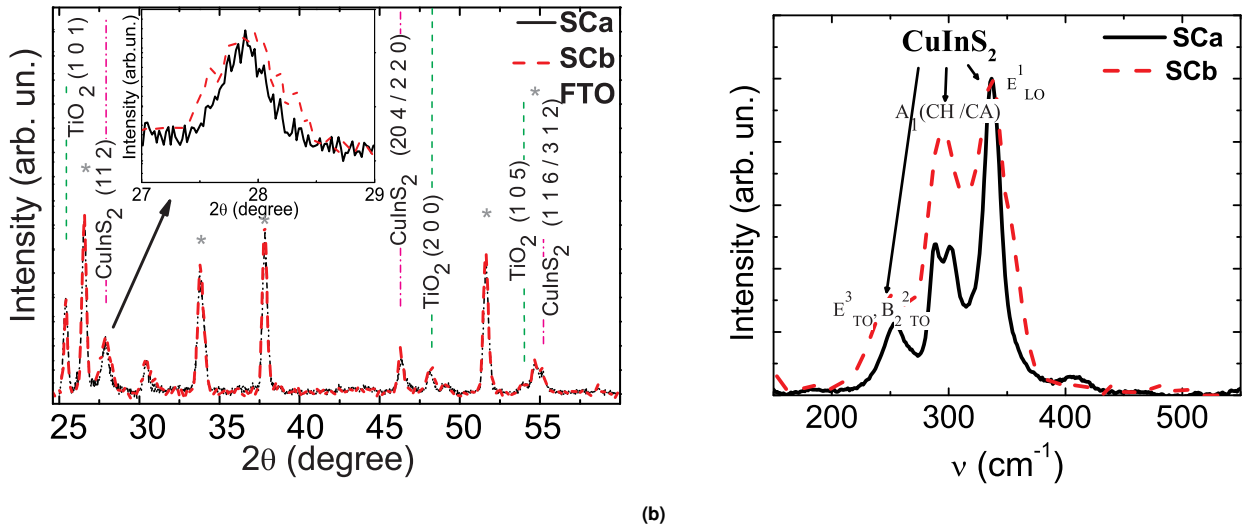

(a) (b)

Fig. 2 (a) GXRD and (b) Raman spectra of solar cells SCa (full line) and SCb cell (dashed line).

and the determination of the characteristic times, different approaches were implemented. The first approach is based on the shape and the presence of only one cycle in the Nyquist plots, so the imaginary parts of the IMVS and IMPS responses ($H''_{IMVS,IMPS}(\omega)$) are expected to exhibit one peak in the $H''_{IMVS,IMPS}(\omega)$ vs. ω representation (or Bode plots). The simplest method to obtain the characteristic time is from the frequency position of the peak in $H''_{IMVS,IMPS}(\omega)$ (defined as $\omega_{peak}^{VS,PS}$). Therefore, $\tau_1^{VS,PS}$ is defined as $\tau_1^{VS,PS} = \frac{1}{\omega_{peak}^{VS,PS}}$. A fitting according to Equation 13 leads to a second expression for the characteristic time $\tau^a_{IMVS,IMPS}$. In this case $\tau^a_{IMVS,IMPS}$ and the amplitude of the signal (A) are fitting parameters

$$H''_{IMVS,IMPS}(\omega) = \frac{-A\omega\tau^a_{IMVS,IMPS}}{1+(\omega\tau^a_{IMVS,IMPS})^2} \quad (16)$$

The second approach relies on a generalization of relaxation-like processes that is commonly observed in DSSC, where the exponent in the denominator of Equation 16 can be substituted by a new fitting parameter $\mathbf{m}$[27], and a third characteristic time ($\tau^b_{IMVS,IMPS}$) is obtained

$$H''_{IMVS,IMPS}(\omega) = \frac{-A\omega\tau^b_{IMVS,IMPS}}{1+(\omega\tau^b_{IMVS,IMPS})^m} \quad (17)$$

Two examples of the $H''_{IMVS,IMPS}(\omega)$ fitting are presented on the Bode plots of Figure 4, Fit_a and Fit_b are the fittings according to Equation 16 and Equation 17 respectively. In this case the values of $\tau_1^{VS,PS}$ were used as initial values for the fittings. For Fit_b $\mathbf{m} = 2$ was also used as initial value for the fitting. A good agreement in the peak determination with both fittings could be observed, in figure 4a for the IMVS response a slightly better fitting could be observed for Fit_a compared with Fit_b. For the IMVS signals fittings of sample SCa the obtained coefficient of determination (R^2 values) were between 0.59 and 0.94 for Fit_a and 0.60 to 0.95 for Fit_b. For SCb the obtained R^2 values for IMVS were between 0.93 to 0.98 for Fit_a and Fit_b. Meanwhile for IMPS data the obtained values were between 0.91 to 0.93 for Fit_a and between 0.94 and 0.96 for Fit_b. In the case of the IMPS response (Figure 4b) Fit_b is in better agreement with the high frequency end of the spectra. This better fitting could be also associated with the higher width of the peak in the IMPS spectrum and the diffusion limited behavior of the cell in the high frequency domain.[27]

As a result of the previous analysis, three different characteristic recombination and transport times were obtained from IMVS and IMPS responses. Figure 5 shows the calculated characteristics times for the SCa solar cell as a function of the illumination intensity I_0. As it can be observed, a very good agreement between the different analyses implemented is achieved. Also, both time constants decrease with the intensity I_0. As the plot is in logarithmic scale, the linear behavior can be associated with a power law commonly observed in DSSC.[26,28,30,33–35] This kind of power law is attributed with an exponential distribution of trap states within the bandgap of the semiconductor electrode.[26,28,30,33–35] Generally, the trapping processes depend on the presence of defect states within the bandgap of the semiconductor (bulk and surface states) and therefore the trapping and detrapping rates will be sensitive to the energy level of the defect states and the occupancy of these defects. If these trap states are involved in the transport dynamics of the charge carriers, the trapping and detrapping rates would be responsible for the time in which the carriers will remain outside the conduction band and therefore they will not contribute to the photocurrent. As the solar cell is illuminated and carriers are photogenerated, the trap states start to participate in the trapping/detrapping process of electrons. Once the stationary regime is reached, some trap states (the lower energy ones) will be filled. Higher values of I_0 will lead to higher ocuppancy defect states. As the number of participating trap states increases, high energy trap states become available and start to be more involved in the trapping/detrapping process. As the rates of the trapping and detrapping processes depend on the energy difference be-

View Article Online
DOI: 10.1039/C9CP04256C

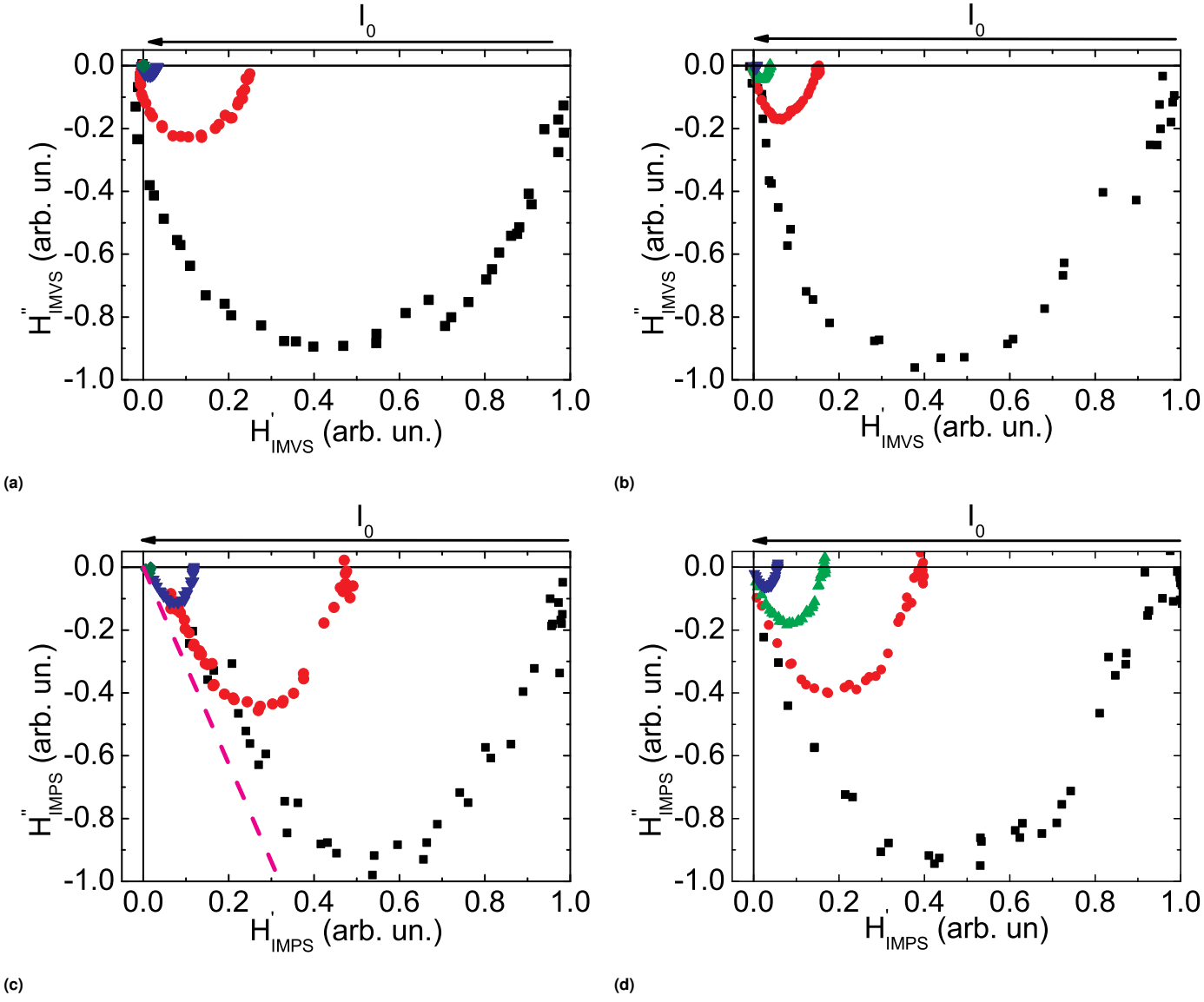

Fig. 3 Nyquist diagrams for the $H_{IMVS,IMPS}(\omega)$ responses of the solar cells for different values of I_0 (a) IMVS response of cell SCa (b) IMVS response of cell SCb (c) IMPS response of cell SCa, (d) IMPS response of cell SCb. In (c) the dashed magenta line is a -45 degree line corresponding with diffusion limited process

View Article Online
DOI: 10.1039/C9CP04256C

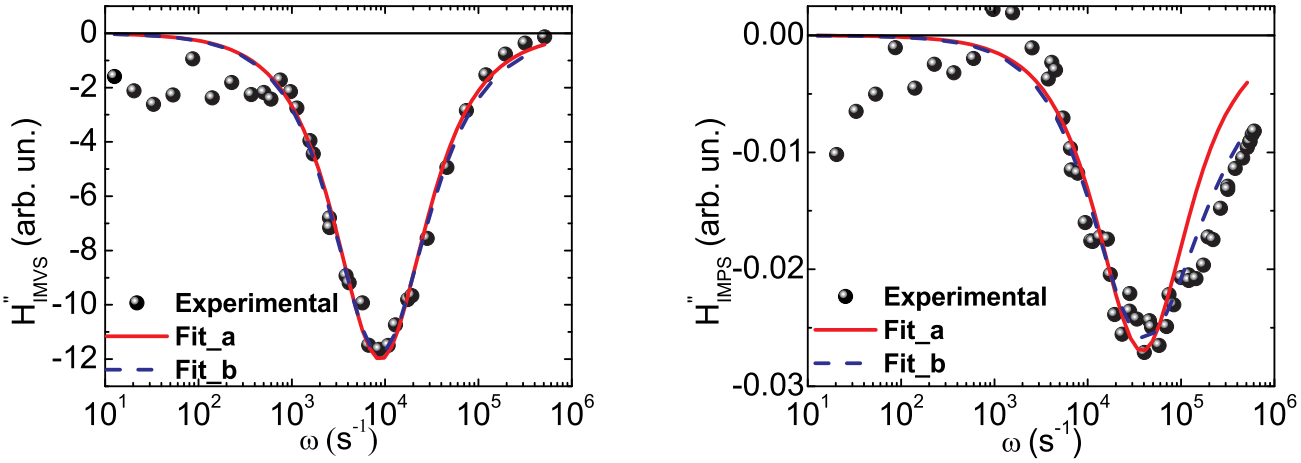

Fig. 4 Imaginary parts of $H_{IMVS,IMPS}(\omega)$ responses of the SCa solar cell and the different implemented fittings. (a) IMVS response (b) IMPS response. The continuous component of the light intensity used is $I_0 = 2.44 mW/cm^2$ for both measurements. The dots are the experimental results, the red solid line is the fitting by Equation 16, and the blue dotted line is the fitting by Equation 17.

tween the conduction band and the defect states, faster rates are expected, these high energy trap states would have faster trapping and detrapping rates,[26,28,30,33–35] leading to faster processes and the consequential decrease in the characteristics times of the solar cell. Both the transport and recombination times had the same behavior with I_0 but they exhibit different slopes. This difference in the slopes leads to a noticeable decrease in the difference between both characteristics times as I_0 increases. In Figure 5b the calculated charge collection efficiency η_{CC} for each characteristic time (η_{CC1}, η_{CC2} and η_{CC3} for $\tau_1^{VS,PS}$, $\tau^a_{IMVS,IMPS}$ and $\tau^b_{IMVS,IMPS}$ respectively) can be observed. As discussed above, the proximity of the characteristic times leads to a decrease in the η_{CC} with I_0.

The results in Figure 5 were used to calculate average IMVS and IMPS characteristic times ($\tau^{VS}_{SCa,SCb}$ and $\tau^{PS}_{SCa,SCb}$ respectively) for SCa and SCb. These average characteristic times are presented in Figure 6a and their corresponding η_{CC} in Figure 6b. In these figures, the dynamics of solar cells SCa and SCb can be compared. As it can be observed, τ^{VS}_{SCa} is almost two times higher than the corresponding time of SCb (τ^{VS}_{SCb}) while τ^{PS}_{SCa} is very close to τ^{PS}_{SCb} for all the optical intensities studied. Figure 6b presents values for η_{CC} (calculated from Figure 6a) and shows that the important difference in the recombination times leads to an attenuation in the collection efficiencies for the SCb cell when compared to cell SCa.

As was previously mentioned, the occupancy dynamics of the defect states could be responsible for the decrease in the characteristic times with I_0 as shown in Figure 6a. Also, the characteristic recombination times of SCa are almost 2 times higher than the times of SCb, indicating a lower density of defect states in SCa. As was previously mentioned, two main differences between both cells are the solution-based deposition technique and the annealing temperature in the final stage of the deposition process. A 500 °C annealing was used for cell SCa while a 250 °C one for cell SCb. As a consequence of these differences, the crystal quality for SCa is higher, as demonstrated by GXRD and Raman spectroscopy for the CIS layer (see Figure 2). Therefore a smaller density of defect states is expected for this cell, both within the bulk of each layer and at interface or at the surface. At least, a different energetic distribution of the defect states can be expected. This difference in the density or distribution of defects states for SCa could be responsible for the higher characteristic recombination times and better charge collection efficiency (Figure 6b) observed.[26,28,30,33–35] Also, the small dependence in the transport times with I_0, with a negligible difference between the two cells, could be associated to a different density of defect states participating during the transport of the carriers in the interior of the cells in comparison with those of the recombination time.[30] The times measured by IMVS and IMPS represent the effective characteristic lifetime and transport time of each cell. They encompass all the present processes which take place in the cell, from the excitation of the electron-hole pair, the charge separation, transport through the CIS layer (for holes) and transport in both the buffer and TiO_2 layers (for electrons). They also include the multitrapping and recombination processes which take place until the final extraction of the carriers. Therefore, intrinsic lifetimes evaluated using both IMVS and IMPS, differ from the lifetime corresponding to each individual stand-alone layer. They are characteristic response times of the device, in real operation conditions, rather than typical time constants of the material. For this reason the measured times are on the order of the millisecond.[28,36]

The previous discussion was performed following the historical development and analysis of both IMVS and IMPS techniques, which is based in the association of the obtained times with the cell recombination and transport times. However, recent experimental evidence points out that charge accumulation and release

View Article Online
DOI: 10.1039/C9CP04256C

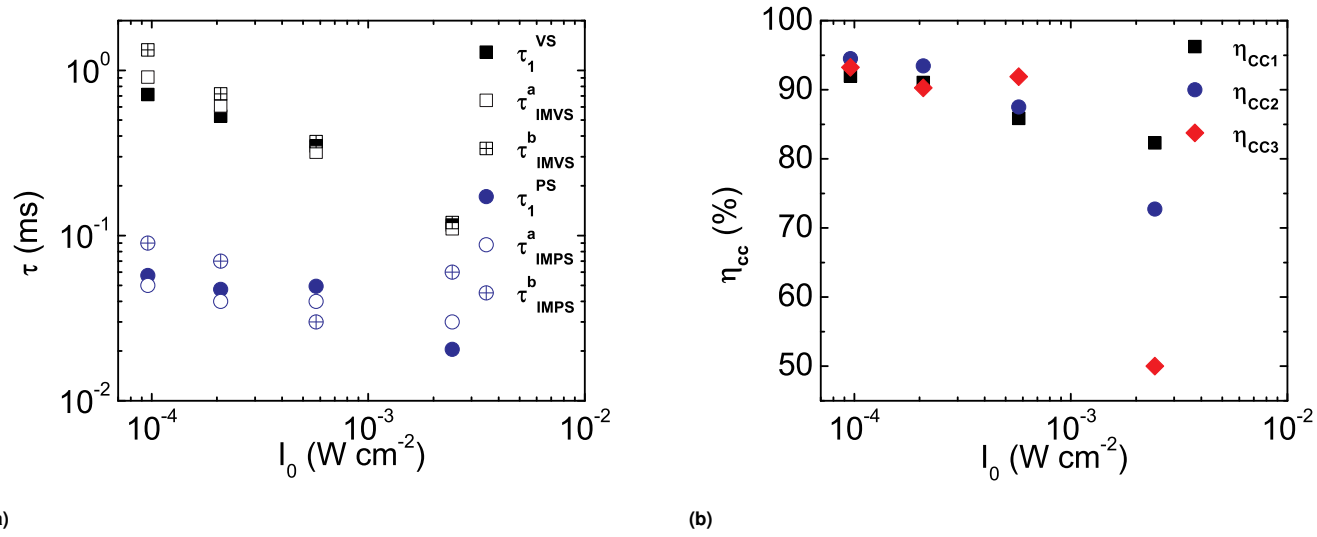

(a) (b)

Fig. 5 (a) Effective times of SCa as obtained from the different analysis implemented for different values of I_0. Effective lifetimes (black squares dots) and effective transit times (blue rounds dots). (b) η_{CC} as calculated from the different characteristics times for different values of I_0

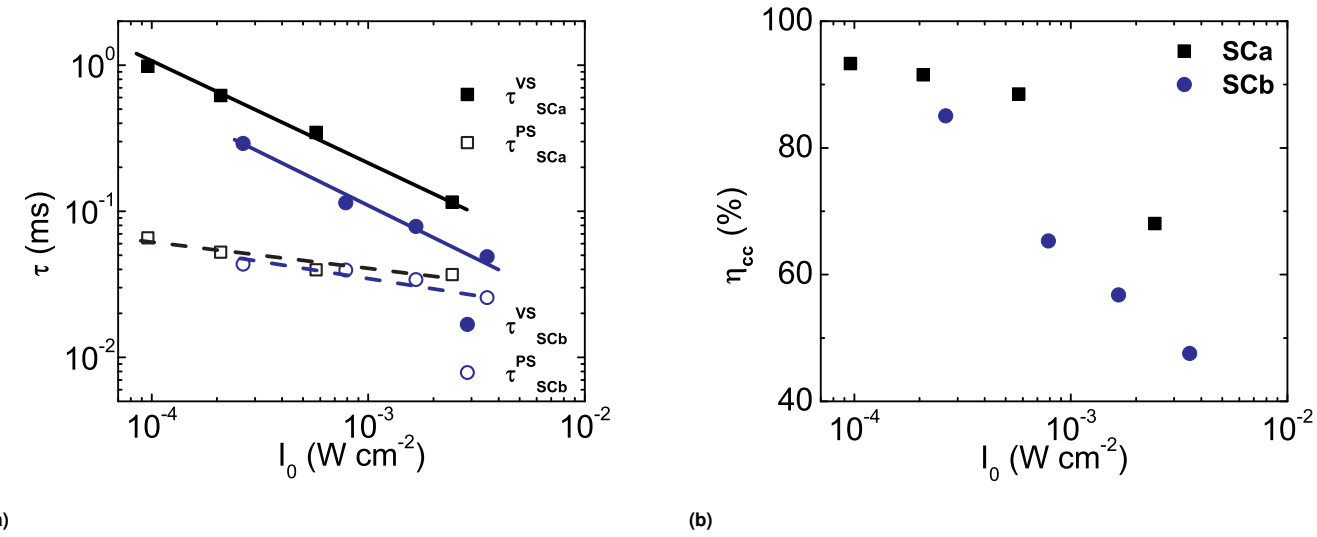

(a) (b)

Fig. 6 (a) Comparison between the characteristics lifetime (full dots) and transport time (hollow dots) of cells SCa (black square dots) and SCb (blue round dots) for different values of I_0. (b) η_{CC} as calculated from the different characteristics times for different values of I_0.

View Article Online
DOI: 10.1039/C9CP04256C

processes could be involved and play a significant role in the observed times.[37–40] Also, transport processes could take place while the IMVS spectra is measured (in spite of the potentiostat imposed open circuit potential condition).[40,41] Even when these transport processes have influence on the observed times, it is possible that they are not entirely dominant in the lifetime determination.[38] Therefore, the influence of such processes make the obtained times not necessarily equal to the bulk charge lifetime and transport times (as usually interpreted) and they are more like *pseudo lifetimes*.[37] Therefore, we emphasize that our previous identification of the characteristic times for both techniques with the bulk lifetime and transport time becomes not entirely accurate. Although the identification of the bulk times is inherently difficult, our obtained times are the characteristic times of the response of the solar cell when excited in real operation conditions. Moreover, the observed times encompass the complexity of the phenomena and processes which take place when the sample is excited and represent the complete characteristic response time of the cell in both open circuit and short circuit condition (for IMVS and IMPS respectively). These response times could be pictured as if in a purely excitation-response system, and this is why we called characteristics lifetime and transport times instead of only lifetime and transport time. They should be considered as the result of the effective response of the samples under the imposed conditions. Therefore, as pointed out during the discussion, every change in the inner structure or the crystalline degree, density of defects or interface quality as a consequence of the thermal treatment (as in our case) should have an effect in the obtained characteristic times as previously discussed. Although, the identification of the measured quantities could be troublesome, the overall better performance of SCa with respect to SCb is clearly observed. In spite of the previous comments on the interpretation of the results the following section develops an analysis and discussion based in the continuity equation. These kind of approaches are very commonly used in DSSC[15,18,19,25–27,29] and allows the discussion of the results in comparison with other results available in the literature. Moreover, while following the results obtained by this analysis makes possible to further discuss the evolution of the relevant parameters of the samples and the influence of their different preparation conditions.

3.1 Analysis from the continuity equation.

Usually different types of solutions to the continuity equation are implemented for the analysis of the IMPS response.[26,30,42] Also, another interesting effect that could be addressed by this approach is the RC attenuation in the IMPS response. This effect is produced by the accumulation of charge carriers in the interface between the conductive glass substrate and the cell.[19,20,28,30,42,43] The accumulation of charge also leads to a capacitive (C) effect in the cell which together with the series resistance (R) becomes a RC circuit element in series with the response of the cell.[19,20,28,30,42,43] Generally, this effect is important in the IMPS response and particularly affects the signal in the high frequency domain. As the measurements are performed in short circuit condition this effect is associated with the glass conductive oxide interface.[43,44] The effect of the RC attenuation produces a modification of the measured $H^{meas}_{IMPS}(\omega)$ which is related with the inner response of the cell ($H^{int}_{IMPS}(\omega)$) by[19,20,28,30,42,43]

$$H^{meas}_{IMPS}(\omega) = H^{int}_{IMPS}(\omega)\frac{1}{1+j\omega RC} \tag{18}$$

Generally, this effect could be minimized if the layer is thin or could be considered negligible when no expansion of the IMPS response to the third quadrant of the complex plane is observed.[25,28,33] As neither of the observed IMPS responses present this kind of expansion in the Nyquist plots, the RC attenuation was not considered in the first part of the analysis, i.e. the calculation of $\tau^{a}_{IMVS,IMPS}$, $\tau^{b}_{IMVS,IMPS}$ and $\tau_1^{VS,PS}$ respectively.

Generally, the fittings of the IMVS and IMPS responses are based on models of the solar cells as formed by one layer. In this case, only one equation is used to model de dynamics of the solar cell[26] (in our case, Equation 9). By this approach, several of the main performance parameters of the solar cell, like diffusion constants, characteristics times and extraction rates can be obtained.[15,18,19,26] As the only difference in the solution of Equation 9 between the IMVS or IMPS case is in the boundary condition (the term depending on k_{sep}), the parameters obtained from the fitting of the IMVS response can be used to simplify the fitting of the IMPS response. Therefore, for the analysis of these responses, a fit of the IMVS response with the solution to Equation 9 was first performed, the fitting parameters were D_e, τ_e, α and the amplitude of the signal. As initial guesses for each fitting parameter, previously measured experimentally values were used.[45,46] As an example τ^{VS}_{SCa} was used for τ_e, α was obtained from previous optical characterizations and thickness determination obtained from a previous work,[46] for D_e an empirical relation with the thickness and τ_{IMPS} was used (see below). Moreover, for the IMPS response, the number of fitting parameters is increased by two: the previous four plus k_{sep} and the RC constant to evaluate the attenuation effect. In this second fit the values of D_e, τ_e, and α previously obtained from the IMVS fit were used as seeds for the IMPS fitting. For the additional parameters k_{sep} and RC, different values similar to those reported in the literature were used as initial values.[19] As can be observed in Figure 7 a good agreement between the experimental results and the model was obtained. Moreover, Figures 8 and 9 show the good accuracy in the determination of the values of the relevant parameters obtained from both the IMVS and IMPS fittings. Figure 7 shows the fittings of the experimental responses of SCa with the solution of Equation 7 for $H''_{IMVS}(\omega)$ (Figure 7a) and the fitting with the solution of Equation 6 for $H''_{IMPS}(\omega)$ response (Figure 7b).

As the parameter τ_e in Equation 9 represents the effective lifetime of the charge carriers in the cell, in the result of the fittings with the solution of Equation 9, the characteristic times obtained from the previous IMVS signal analysis (τ^{VS}_{SCa}) were compared. In Figure 8a the times obtained from the fitting of the SCa cell could be observed (τ_e^{VS} and τ_e^{PS}, as obtained from the fit of the IMVS or IMPS signals respectively). Figure 8b presents the same results for cell SCb. A very good agreement is evident between the results by both analysis strategies for the IMVS fit of both cells. However, an important difference can be observed for the IMPS analysis on

View Article Online
DOI: 10.1039/C9CP04256C

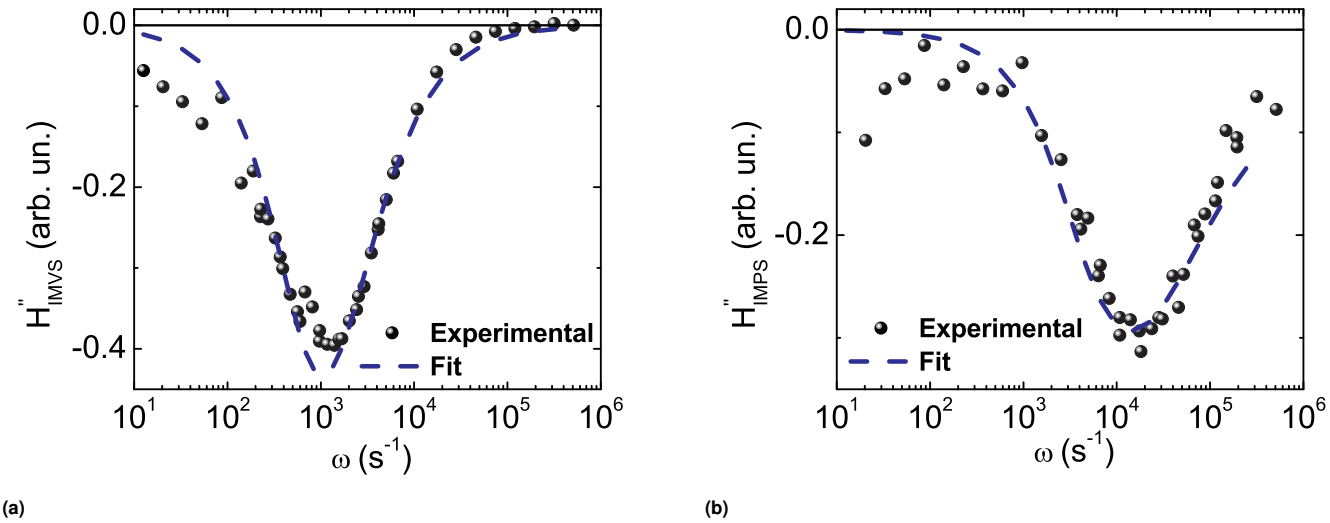

Fig. 7 Imaginary parts of $H_{IMVS,IMPS}(\omega)$ responses of the SCa solar cell, compared to the fitting with the solutions of the continuity equation.The black dots represent the experimental results and the blue dashed line is the fitting curve (a) IMVS response (b) IMPS response. The continuous component of the light intensity used is $I_0 = 2.44 mW/cm^2$ for both measurements as in Figure 4.

cell SCa. In contrast, for cell SCb both results are very close to the previous analysis. In spite of the discrepancy, the same behavior of the characteristic times with I_0 is obtained for both the IMVS and the IMPS fits. The very good agreement between the different results is a good indicator of the suitability of this analysis and procedure to study the recombination and transport dynamics of solar cells.

Considering the good agreement between the fittings, more parameters of the cell can be studied. Figure 9 shows values obtained for D_e for cell SCa (Figure 9a) and cell SCb (Figure 9b). As was the case with the lifetime, a very good agreement is obtained for the two fittings of cell SCb and, again a bigger difference is observed for cell SCa. Also, it has been reported that the diffusion constants follow a linear behavior with the reciprocal of the transport time of the cells.[45,47]

$$D_e = \frac{d^2}{\kappa \tau_{IMPS}} \tag{19}$$

Here **d** is the thickness of the cell and κ a constant.[45,47] The insets in Figure 9 are the plots of D_e as a function of the reciprocal of the transport time, where a good agreement with the linear behavior can be observed. Again, a very good fitting can be obtained for cell SCb while the results for cell SCa are more disperse. However, both cells present an increase in the diffusion constant with the intensity I_0. A comparison between cells revels that the diffusion constant for cell SCb is higher than that for cell SCa, in agreement with the shape of the IMPS Nyquist plot. As the diffusion constant is higher for cell SCb, it is less probable that the cell exhibits the diffusion limited behavior characterized by the linear slope in Figure 3.

Finally, Table 1 presents the remaining fitting parameters that can be obtained from the IMPS fittings for the different I_0 values, also the R^2 values and the the square-root of the sum of squares of residuals (sqres) are reported. The results for k_{sep} are in good agreement with the shape of the Nyquist plots of the IMPS signal already present in Figure 3, i.e. the 45 degree slope linear behavior at high frequencies. The values of k_{sep} for cell SCa are several orders of magnitude higher than the ones corresponding to cell SCb. Also, the small values of the RC constants (compared with the corresponding times) obtained for both cells indicate that the RC attenuation effect is negligible in these samples.[42] Also, a really good agreement is obtained for the values of the absorption coefficient of each cell. The main discrepancies observed for the results on SCa between the IMVS and IMPS fittings could be associated with the differences on the shape of the IMVS response of this cell. The diffusion limited behavior of this cell leads to a higher impact of k_{sep} in the calculated parameters. The predominance of this parameter and the departure for the semicircular shape in the Nyquist plots leads to higher uncertainty on the implemented fitting.

Although this strategy of multiple parameter fitting is hard to implement and could lead to results without physical meaning, the different verifications of the parameters and the good general agreement between the results gives us confidence in the implemented procedure. The results of the photovoltaic device characterization for both SCa and SCb can be observed in Table 2.[46] A higher conversion efficiency (η) for cell SCa is observed in concordance with the previous results on the charge collection efficiency η_{CC}. As previously mentioned, the differences in the growth technique and post treatment implemented in SCa with respect to SCb could lead to a better overall crystal quality of SCa. This increased crystallinity could lead to a reduced defect state density in each individual layer of SCa. Also, a better layer quality could help the transport of holes in the $CuInS_2$ layer and of electrons in the TiO_2 layer.[28] Besides, a better interface/surface quality or a better integration of the buffer layer in the cell could

View Article Online
DOI: 10.1039/C9CP04256C

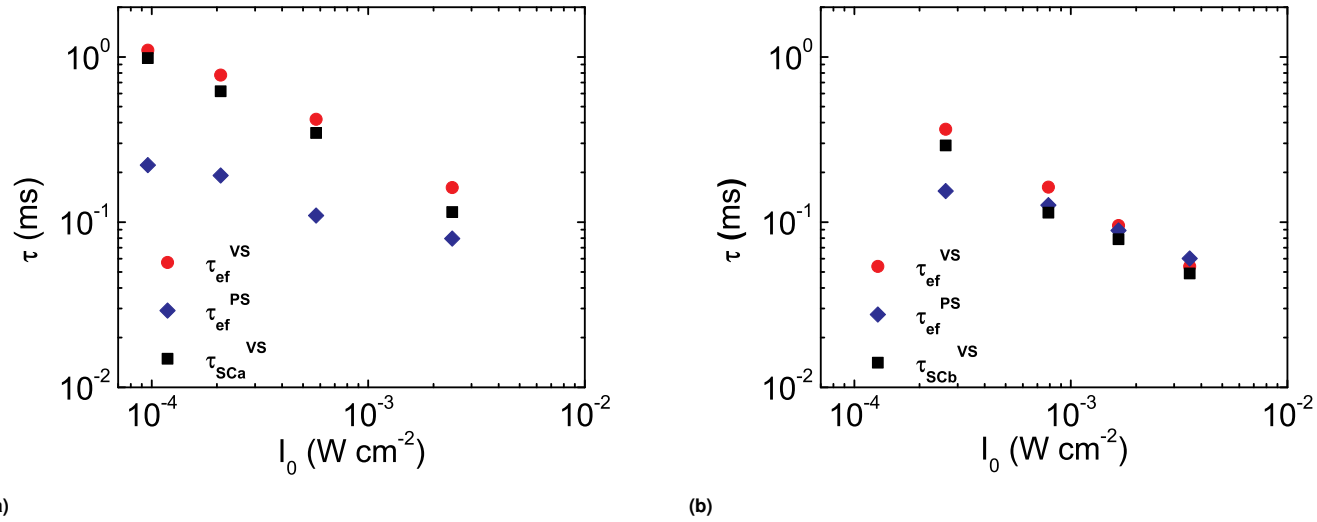

Fig. 8 Comparison between lifetime constants obtained by fitting the continuity equation of IMVS data (τ_e^{VS}) and IMPS data (τ_e^{PS}) with the one obtained from IMVS by the average method of Figure 6a for (a) cell SCa, (b) cell SCb.

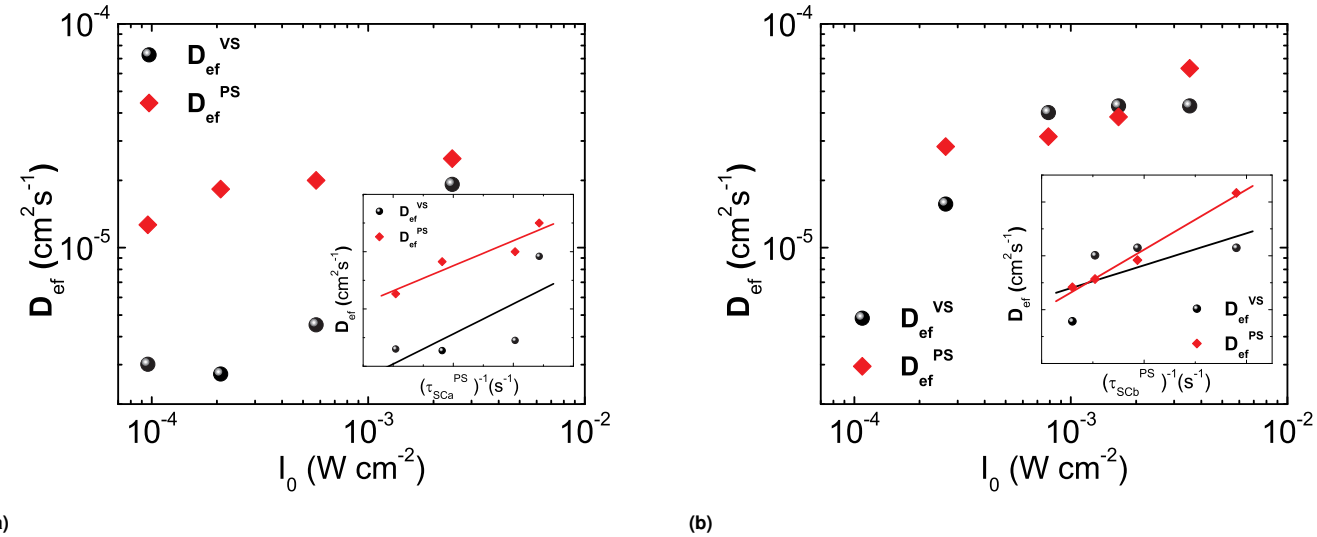

Fig. 9 Effective Diffusion constant of cells SCa and SCb (a and b respectively), calculated from the fittings of IMVS and IMPS responses for different values of I_0. The inset in each figure presents the diffusion constants as a function of the reciprocal of the transport times (the lines are guidelines).

Table 1 Parameters associated with the fitting of the solution of the continuity equation with the experimental data of both solar cells.

Cell	I_0 (mW/cm^2)	τ_{ef} (ms)	k_{sep} (s^{-1})	RC (ms)	α (cm^{-1})	R^2	sqres (arb. un.)
SCa	0.26	0.191	1.67×10^{4}	1×10^{-4}	1.27×10^{4}	0.955	1.79×10^{-1}
	0.78	0.221	9.07×10^{3}	1×10^{-4}	1.24×10^{4}	0.988	5.67×10^{-2}
	1.66	0.110	1.14×10^{4}	1×10^{-5}	1.30×10^{4}	0.984	4.53×10^{-2}
	3.54	0.079	1.52×10^{4}	1×10^{-5}	1.32×10^{4}	0.851	5.18×10^{-1}
SCb	0.26	0.154	5.16	2.55×10^{-4}	1.39×10^{4}	0.979	9.53×10^{-2}
	0.78	0.063	4.32	1×10^{-5}	1.39×10^{4}	0.986	6.25×10^{-2}
	1.66	0.127	3.43	1.55×10^{-4}	1.39×10^{4}	0.988	6.08×10^{-2}
	3.54	0.089	3.30	1×10^{-5}	1.39×10^{4}	0.985	6.28×10^{-2}

View Article Online
DOI: 10.1039/C9CP04256C

lead to an overall enhancement of the transport within the cell and the reduction of the recombination centers.[28,42,48]

Table 2 Photovoltaic performance parameters for both solar cells.

Cell	V_{OC} (mV)	J_{SC} (mA/cm^2)	η (%)
SCa	583	17.7	3.3
SCb	240	21.7	1.84

4 Conclusions

The modeling of the modulated photovoltage and photocurrent responses of two different solid state solar cells prepared in superstrate configuration was successfully implemented from the solution of the continuity equation for a one layer cell by fitting both IMVS and IMPS data for each cell. The comparison and good agreement between the different analysis of the IMVS and IMPS data that are typically used in DSSC shows the viability of the implemented fittings in solid-state and thin-film solar cells. Moreover, using this analysis, additional parameters as the diffusion constants can be obtained. Further improvements or additional parameters can also be incorporated to this approach by taking advantage of both fittings. As the dynamics of the photogenerated charge carriers is highly dependent on the presence and distribution of defect states, the structural order or crystalline degree of the materials is determinant for the resulting optoelectronic properties. For the samples under study, the dynamics of the solar cells shows a better performance in cell SCa compared with SCb, mainly observed in the different recombination times of the cells. This better performance can be associated with a higher crystalline quality of the layers and interface in cell SCa. Also, it could be observed from the IMPS spectra, that the dynamic in cell SCa is diffusion limited while for cell SCb is kinetically limited. This higher crystallinity of cell SCa is associated both to the higher temperature of the thermal treatment and to solution-based deposition method. The high crystal quality was also confirmed by the GXRD and Raman spectroscopy. A dependence of the time constant with illumination intensity was attributed to changes in the filling of defect states with intensity. Meanwhile, the corresponding dependence of the diffusion constant was attributed to its relation with the transport time. Also, a better photovoltaic performance of cell SCa compared to SCb was observed confirming a better carrier transport within SCa.

5 Materials & Methods

5.1 Cell Preparation

The two $TiO_2/In_2S_3/CuInS_2$ superstrate cells were synthesized using fluorine doped tin oxide (FTO, Libbey Owens Ford, TEC 8/3 mm) as substrate. The TiO_2 and In_2S_3 layers were deposited layer by layer using the spray pyrolysis technique. Details of precursor-solutions preparation can be found elsewhere.[46,49,50] The TiO_2 layer was deposited over a hot plate at 350 °C, spraying 10 cycles of 20 s of duration with 60 s pauses between cycles. After the deposition process, the samples were maintained at 450 °C on the hot plate during 60 min and cooled at room temperature. Then the In_2S_3 layer was deposited at 300 °C applying 30 s cycles and maintaining the samples in the hot plate for 30 min. Finally, the samples were cooled at room temperature. For the $CuInS_2$ layer, two different growth techniques were implemented: electrodeposition for sample SCa and inks deposited by spin coating for sample SCb. The electrodeposition was performed following the procedure described elsewhere.[51] Briefly, the deposition of the CIS films was carried out using a standard three-electrode cell; a saturated calomel electrode (SCE) and a Pt mesh as reference and counter electrodes respectively. A constant potential of -1.2 V vs SCE for 60 minutes was applied using an electrolytic bath at 30 °C containing 0.01 mol L^{-1} $CuCl_2$, 0.01 mol L^{-1} $InCl_3$, 0.50 mol L^{-1} Na_2SO_3 and 0.2 mol L^{-1} $Na_3C_3H_5O(COO)_3$. The pH value was adjusted to 8 by the addition of HCl or NaOH from stock solutions. The sample was annealed at 500 °C for 60 min after the deposition. Finally, a chemical etching was performed over the sample with KCN (0.25 mol/L) for 30 seconds. In the case of sample SCb, the $CuInS_2$ layer was deposited by spin coating from a solution of CuCl (0.105 mmol), $InCl_3$ (0.1 mmol), and thiourea (0.4 mmol) in a mixture of acetic acid and N-propylamine (0.046 and 0.6 mL respectively). Two spin coating cycles were used and, between the cycles a 10 min thermal treatment at 150 °C was used. Finally a second 10 minutes thermal treatment was performed at 250 °C.[46,49,50] The final architecture of the cell is observed in Figure 10. The electrical contacts were painted with conductive graphite ink (Alpha Aesar).[46,49,50]

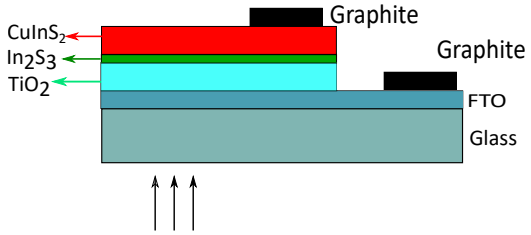

Fig. 10 Diagram of the solar cells under analysis. Samples SCa and SCb differ in the deposition method used for the CIS layer. Furthermore, the main difference between both cells is the annealing temperature: cell SCa was annealed at 500 °C and etched in contrast to annealing at 250 °C for cell SCb.

5.2 Morphological Characterization

The structure and crystalline degree of the films were analyzed by grazing incidence X-ray diffraction (GXRD) with a PANalytical X'Pert Pro diffractometer, Cu-Kα (λ=1.541 Å) radiation at 40 kV and 40 mA. The difractograms were registered scanning the samples between 20° and 70° at 0.02 °/s. The crystallographic data for each phase were compared with those from the literature and analyzed with X'PertHighScore software. Localized Raman spectroscopy was used as a complementary technique. The spectra were recorded with an Invia Reflex confocal Raman microprobe. The measurements were carried out with a 785 nm excitation laser and in backscattering configuration using a 50x objective.

5.3 Photovoltaic Characterization

Current-Voltage curves where recorded in the dark and under simulated solar air-mass filter 1.5G illumination with a solar simu-

View Article Online
DOI: 10.1039/C9CP04256C

lator (Oriel-Newport 69907). The photocurrent was measured with an IVIUM compact potentiostat. In order to evaluate the efficiency of the different devices the light intensity was calibrated with a Si photodiode.

5.4 IMVS and IMPS Characterization

In order to measure the IMVS and IMPS responses, a 7 mW modulable red laser λ = 635 nm (Coherent LabLaser C MVP) was used as the source of optical excitation. The modulated signal was controlled by a signal generator (Tektronix AFG 3022B). A sine waveform was selected to control the laser. The modulation was carefully selected in order to obtain a sinusoidal optical light intensity signal. Moreover, the modulation part (I_A) to mean value (I_0) ratio was fixed close to 10 % (i.e. $\frac{I_A}{I_0} \approx 0.1$). In this configuration, different frequency sweeps were performed in the 1 to 100 kHz frequency range. Moreover, different values of were used keeping the amplitude relation close to 10%. A beam splitter divided the excitation and part of the signal was measured by a fast photodiode and used to evaluate the excitation signal. Also the continuous component exciting the sample I_0 was measured with a Radiant Power Meter (Oriel 70260). The response of the samples was measured with a potentiostat (Teq4), which also set the working conditions to open circuit and short circuit for the measurement of IMVS and IMPS respectively. The responses were converted in the A/D converter of the potentiostat and redirected to a Lock-in amplifier (Stanford Research Systems SRS-530), which measured the amplitude and relative phase of the modulated signal of each sample and photodiode signals ($\phi_{sample}(\omega)$ and $\phi_{pd}(\omega)$ respectively). In this way the IMVS and IMPS response ($H_{IMVS,IMPS}(\omega)$) of the sample was calculated as

$$H_{IMVS,IMPS}(\omega) = \frac{\phi_{sample}^{IMVS,IMPS}(\omega)}{\phi_{pd}^{IMVS,IMPS}(\omega)} \frac{1}{I_0} \quad (20)$$

I_0 was used as a normalization factor for comparison purposes. Finally, the sinusoidal character of the optical excitation signal was checked with the photodiode as the generated photocurrent was observed with an oscilloscope (Tektronix TDS210) after being amplified by a current preamplifier (Stanford Research Systems SRS SR570). In all the measurements, the incidence of the optical signal on the sample was through the substrate side (the glass/FTO side).

Conflicts of interest

There are no conflicts to declare.

Acknowledgements

The Uruguayan authors are grateful to PEDECIBA-Física Uruguay, ANII (Agencia Nacional de Investigación e Innovación) projects FSE_1_2014_1_102184 and FCE_1_2014_1_104739, CSIC (Comisión Sectorial de Investigación Científica) and CAP (Comisión Académica de Posgrado) of the Universidad de la República. The Argentinean authors acknowledge the financial support from CONICET-ANII (MOV_CO_2013_1_100005), ANPCyT (PICT 972/15), and Universidad Nacional de Mar del Plata (ING477/16).

Notes and references

1 C. S. Schnohr, *Appl. Phys. Rev.*, 2015, **2**, 031304.
2 S. H. Wei and A. Zunger, *J. Appl. Phys.*, 1995, **78**, 3846–3856.
3 M. Turcu, I. M. Kötschau and U. Rau, *J. Appl. Phys.*, 2002, **91**, 1391–1399.
4 R. Scheer, H. W. H.-W. Schock and Wiley InterScience (Online service), *Chalcogenide photovoltaics : physics, technologies, and thin film devices*, Wiley-VCH, 2011, p. 368.
5 Y. Ogawa, S. Uenishi, K. Tohyama and K. Ito, *Sol. Energy Mater. Sol. Cells*, 1994, **35**, 157.
6 S. P. Grindle, C. W. Smith and S. D. Mittleman, *Appl. Phys. Lett.*, 1979, **35**, 24–26.
7 J. Herrero and J. Ortega, *Sol. Energy Mater.*, 1990, **20**, 53–65.
8 W. Shockley and H. J. Queisser, *J. Appl. Phys.*, 1961, **32**, 510–519.
9 F. Jacob, N. Barreau, S. Gall and J. Kessler, *Thin Solid Films*, 2007, **515**, 6028–6031.
10 A. H. Cheshme khavar, A. Mahjoub, F. S. Samghabadi and N. Taghavinia, *Mater. Chem. Phys.*, 2017, **186**, 446–455.
11 A. H. Cheshmekhavar, A. R. Mahjoub, H. Fakhri and M. Dehghani, *RSC Adv.*, 2015, **5**, 97381–97390.
12 A. H. Cheshme Khavar, A. R. Mahjoub, F. Tajabadi, M. Dehghani and N. Taghavinia, *Eur. J. Inorg. Chem.*, 2015, **2015**, 5793–5800.
13 M. Dehghani, A. Behjat, F. Tajabadi and N. Taghavinia, *J. Phys. D. Appl. Phys.*, 2015, **48**, 115304.
14 L. Peter, E. Ponomarev and D. Fermín, *J. Electroanal. Chem.*, 1997, **427**, 79–96.
15 E. A. Ponomarev and L. M. Peter, *J. Electroanal. Chem.*, 1995, **396**, 219–226.
16 E. A. Ponomarev and L. M. Peter, *J. Electroanal. Chem.*, 1995, **397**, 45–52.
17 G. Schlichthörl, S. Y. Huang, J. Sprague and A. J. Frank, *J. Phys. Chem. B*, 1997, **101**, 8141–8155.
18 G. Schlichthörl, N. G. Park and A. J. Frank, *J. Phys. Chem. B*, 1999, **103**, 782–791.
19 L. Dloczik, O. Ileperuma, I. Lauermann, L. M. Peter, E. A. Ponomarev, G. Redmond, N. J. Shaw and I. Uhlendorf, *J. Phys. Chem. B*, 1997, **101**, 10281–10289.
20 J. Krüger, R. Plass, M. Grätzel, P. J. Cameron and L. M. Peter, *J. Phys. Chem. B*, 2003, **107**, 7536–7539.
21 J. Halme, *Phys. Chem. Chem. Phys.*, 2011, **13**, 12435.
22 L. Bertoluzzi and J. Bisquert, *J. Phys. Chem. Lett.*, 2017, **8**, 172–180.
23 D. Klotz, D. S. Ellis, H. Dotan and A. Rothschild, *Phys. Chem. Chem. Phys.*, 2016, **18**, 23438–23457.
24 J. Li and L. Peter, *J. Electroanal. Chem.*, 1985, **193**, 27–47.
25 L. Peter and K. Wijayantha, *Electrochim. Acta*, 2000, **45**, 4543–4551.
26 B. van der Zanden and A. Goossens, *J. Phys. Chem. B*, 2000, **104**, 7171–7178.
27 F. Wang, Y. Chen, G. Han, Q. Zhang and Q. Ma, *Curr. Appl. Phys.*, 2016, **16**, 1353–1363.

View Article Online
DOI: 10.1039/C9CP04256C

28 C. Grasso, M. Nanu, A. Goossens and M. Burgelman, *Thin Solid Films*, 2005, **480-481**, 87–91.
29 L. Peter, *Electrochem. commun.*, 1999, **1**, 576–580.
30 A. B. F. Martinson, J. E. McGarrah, M. O. K. Parpia and J. T. Hupp, *Phys. Chem. Chem. Phys.*, 2006, **8**, 4655.
31 S. M. Waita, B. O. Aduda, J. M. Mwabora, C. G. Granqvist, S. E. Lindquist, G. A. Niklasson, A. Hagfeldt and G. Boschloo, *J. Electroanal. Chem.*, 2007, **605**, 151–156.
32 L. Bertoluzzi and S. Ma, *Phys. Chem. Chem. Phys.*, 2013, **15**, 4283.
33 A. C. Fisher, L. M. Peter, E. A. Ponomarev, A. B. Walker and K. G. U. Wijayantha, *J. Phys. Chem. B*, 2000, **104**, 949–958.
34 W. Hu, T. Liu, Y. Guo, S. Luo, H. Shen, H. He, N. Wang and H. Lin, *J. Electrochem. Soc.*, 2015, **162**, H747–H752.
35 E. Guillén, L. M. Peter and J. A. Anta, *J. Phys. Chem. C*, 2011, **115**, 22622–22632.
36 R. O'Hayre, M. Nanu, J. Schoonman and A. Goossens, *Nanotechnology*, 2007, **18**, 055702.
37 D. Kiermasch, A. Baumann, M. Fischer, V. Dyakonov and K. Tvingstedt, *Energy Environ. Sci.*, 2018, **11**, 629–640.
38 T. Du, J. Kim, J. Ngiam, S. Xu, P. R. F. Barnes, J. R. Durrant and M. A. McLachlan, *Adv. Funct. Mater.*, 2018, **28**, 1801808.
39 M. C. Heiber, T. Okubo, S.-J. Ko, B. R. Luginbuhl, N. A. Ran, M. Wang, H. Wang, M. A. Uddin, H. Y. Woo, G. C. Bazan and T.-Q. Nguyen, *Energy Environ. Sci.*, 2018, **11**, 3019–3032.
40 M. Neukom, S. Züfle, S. Jenatsch and B. Ruhstaller, *Sci. Technol. Adv. Mater.*, 2018, **19**, 291–316.
41 R. A. Street, *Phys. Rev. B*, 2011, **84**, 075208.
42 T. Oekermann, D. Zhang, T. Yoshida and H. Minoura, *J. Phys. Chem. B*, 2004, **108**, 2227–2235.
43 G. Franco, *Electrochem. commun.*, 1999, **1**, 61–64.
44 C. Chen, R. Peng, H. Wu and M. Wang, *J. Phys. Chem. C*, 2009, **113**, 12608–12614.
45 E. Guillén, F. J. Ramos, J. A. Anta and S. Ahmad, *J. Phys. Chem. C*, 2014, **118**, 22913–22922.
46 Y. Di Iorio and M. Vázquez, *Mater. Res. Express*, 2017, **4**, 045903.
47 J. van de Lagemaat and A. J. Frank, *J. Phys. Chem. B*, 2001, **105**, 11194–11205.
48 C. Grasso and M. Burgelman, *Thin Solid Films*, 2004, **451**, 156–159.
49 Y. Di Iorio, M. Berruet, D. L. Gau, E. L. Spera, C. J. Pereyra, R. E. Marotti and M. Vázquez, *Phys. Status Solidi Appl. Mater. Sci.*, 2017, **214**, 1700191.
50 M. Berruet, Y. Di Iorio, C. J. Pereyra, R. E. Marotti and M. Vázquez, *Phys. Status Solidi - Rapid Res. Lett.*, 2017, **11**, 1700144.
51 Y. Di Iorio, M. Berruet, W. Schreiner and M. Vázquez, *J. Appl. Electrochem.*, 2014, **44**, 1279–1287.

View Article Online
DOI: 10.1039/C9CP04256C

$CuInS_2$ Solar Cells Intensity Modulated Photovoltage and Photocurrent Spectroscopy data were modeled and fitted with the solution of the continuity.